

PROCEEDINGS OF SPIE

SPIDigitalLibrary.org/conference-proceedings-of-spie

Modeling movement artefacts in handheld laser speckle contrast perfusion imaging: influence of wavefront types

Chizari, Ata, Tsong, Wilson, knop, Tom, Steenbergen, Wiendelt

Ata Chizari, Wilson Tsong, Tom knop, Wiendelt Steenbergen, "Modeling movement artefacts in handheld laser speckle contrast perfusion imaging: influence of wavefront types," Proc. SPIE 11959, Dynamics and Fluctuations in Biomedical Photonics XIX, 1195905 (2 March 2022); doi: 10.1117/12.2609849

SPIE.

Event: SPIE BiOS, 2022, San Francisco, California, United States

Modeling movement artefacts in handheld laser speckle contrast perfusion imaging: influence of wavefront types

Ata Chizari^{*a,b}, Wilson Tsong^{a,b}, Tom Knop^a, Wiendelt Steenbergen^a

^aBiomedical Photonic Imaging, Technical Medical Centre, Faculty of Science and Technology, University of Twente, PO Box 217, 7500 AE Enschede, The Netherlands;

^bThese authors contributed equally to this work.

ABSTRACT

Movement artefacts distort handheld measurements of laser speckle contrast imaging (LSCI). Enabling a robust LSCI in handheld use brings convenience for both patients and clinical staff. However, there is a lack of a comprehensive model that can predict and potentially compensate the amount of movement artefacts occurring during a handheld LSCI measurement. Here, we propose an analytical-numerical model based on the optical Doppler effect for handheld LSCI in case of translation on a high scattering static surface. The model incorporates the type of illumination as well as the imaging geometry by taking into account the spread of wavevectors for illumination and detection. We validate the theoretical model by simulated dynamic speckles and experiments for the cases of (1) planar and spherical waves illumination and (2) scrambled waves illumination. Results of the speckle simulation are in agreement with predictions of the numerical model for semi-circular form of the density functions of the incoming and outgoing wavevectors.

Keywords: Analytical models, biomedical optical imaging, computer simulation, Doppler effect, laser speckle contrast imaging, motion artifacts, model-driven development, numerical analysis

1. INTRODUCTION

Laser speckle contrast imaging (LSCI) is a noninvasive method for evaluation of microcirculatory blood flow [1]. It offers several medical applications including dermatology [2], intra/post operative flap surgery [3] and burn wounds [4]. Commercially available LSCI systems are bulky and operate in mounted modality. The former limits their application in operation theatres and other clinical contexts with space limitation while the latter brings inconvenience for both patients and clinicians [5]. Such limitations give rise to develop handheld and compact devices for LSCI. As opposed to all the benefits a handheld LSCI system offers, it can lead to unreliable measurement results due to the involuntarily movements applied during a measurement either by the patient [6] or by the operator [7]. This is due to the high level of speckle sensitivity to any source of movements. When a handheld LSCI measurement is operated, movement artefacts show their influence in causing higher perfusion than its actual level due to extra motion of the speckle patterns within the exposure time (see Figure 1).

In a previous study, we showed that employing an appropriate spatial alignment algorithm, the temporally averaged perfusion maps in mounted and handheld modalities are similar in a visual basis although the movement induced perfusion differences are statistically significant [8]. Therefore, there is a need to model movement artefact so that their occurrence can be prevented and/or compensated. In other studies, we experimentally showed that movement artefacts caused by translation depend on the optical properties of the medium [9] as well as the type of illumination [10]. In this work, we use the concept of optical Doppler effect to predict speckle contrast drop due to linear motion, and for static objects. This is a first step in modelling movement artefacts due to linear motion and rotation when measuring on objects with internal motion, such as perfused tissue.

2. MODEL OF THE OPTICAL SYSTEM

Consider a solid object of very high scattering level (e.g. a white matte surface) moving with a constant velocity \vec{v} along the $x - y$ plane (see Figure 2(a)). For a given point on the object's surface, a cone of base radius r_i is formed that is defined by the range of incoming wavevectors \vec{k}_i . Assuming a lens collecting scattered light, a cone of base radius r_s defined by

*a.chizari@utwente.nl; phone 31 534 891 225; atachizari.com

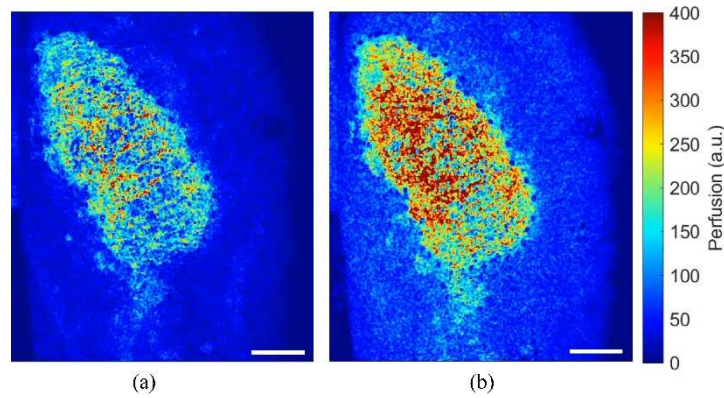


Figure 1 Demonstration of movement artefacts in handheld laser speckle contrast perfusion imaging in a psoriasis lesion on a human lower arm. Scale bars, 2 cm. A single perfusion map acquired with an exposure time of 10 ms during a handheld operation with (a) low and (b) high magnitudes of applied movements. An increased level of measured perfusion is observed in (b) compared to (a) due to the movement artefacts.

the range of wavevectors \vec{k}_s of detected light will be formed. The collected light will cause a time varying intensity $I(t)$ containing a range of frequencies that are assumed here to be dictated by the optical Doppler effect as [11]

$$\omega_D = \vec{v} \cdot (\vec{k}_s - \vec{k}_i). \quad (1)$$

If the bases of illumination and detection cones are mapped on the $x - y$ plane and assuming that the angles between the normal to the surface and both \vec{k}_i and \vec{k}_s is relatively small, then the two circular-shape collections for $\vec{k}_i(x, y)$ and $\vec{k}_s(x, y)$ can be introduced as shown in Figure 2(b). A Doppler histogram is made by adding all the single Doppler shifts as

$$A\left(\frac{\omega_D \lambda}{2\pi V}\right) = p_{R-i}\left(\frac{\omega_D \lambda}{2\pi V}\right) * p_{R-s}\left(\frac{\omega_D \lambda}{2\pi V}\right), \quad (2)$$

where $*$ denotes the convolution operator, $p_{R-i}(\cdot)$ and $p_{R-s}(\cdot)$ are probability density functions of the spreads of incoming and outgoing wavevectors, respectively.

We define the following form for a semicircular form of the density function

$$p_{-i,s}\left(\frac{\omega_D \lambda}{2\pi V}\right) = \frac{\lambda}{\pi^2 V \chi_{i,s}} \sqrt{1 - \left(\frac{\omega_D \lambda}{2\pi V \chi_{i,s}}\right)^2}, \quad (3)$$

where χ_i and χ_s are shape parameters that control the spread of p_{R-i} and p_{R-s} , respectively (see Figure 2(c)). In Figure 2(d) intensity of a simulated speckle frame is shown.

The normalized intensity autocorrelation is calculated by inverse Fourier transforming the power spectral density, that is the auto-correlation of the optical density function introduced in (2), which takes the form

$$g^2(\tau) = 16b_i b_s \left(\frac{J_1\left(\frac{\tau}{b_i}\right) J_1\left(\frac{\tau}{b_s}\right)}{\tau^2} \right)^2 + 1. \quad (4)$$

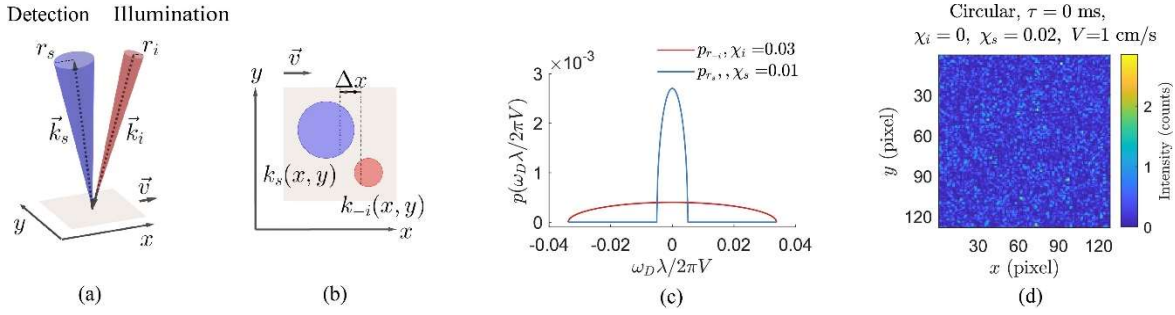


Figure 2 Schematic diagram of the optical system model in which linear translation of a solid object along the $x - y$ plane is assumed. (a) Illumination and detection on a solid object of very high scattering levels (matte surface). (b) Top view of the schematic diagram showing the mapping of the bases of the illumination and detection cones on the object's surface. (c) Density functions for incoming and outgoing wavevectors. $\lambda = 671$ nm; $V = 5$ mm/s. Case of semi-circular shapes for p_{R-i} and p_{R_s} are shown and the density functions for the wavevectors are semi-circular. (d) Representative intensity of simulated speckles on the detector. $\chi_i = 0$ simulates spherical or planar waves for the illuminating beam, while $\chi_i > 0$ simulates scrambled waves. (a-c) are reprinted from [12], chapter 4.

where $J_1(\cdot)$ is the Bessel function of the first kind [13] and $b_{i,s} = \lambda / (2\pi V \chi_{i,s})$. Finally, the contrast of the time integrated intensity as a function of the normalized intensity correlation function has been calculated as

$$C^2 = \frac{32b_i b_s}{T} \int_0^T \frac{1}{\tau^4} J_1\left(\frac{\tau}{b_i}\right)^2 J_1\left(\frac{\tau}{b_s}\right)^2 \left[1 - \frac{\tau}{T}\right] d\tau. \quad (5)$$

Equation (5) cannot be solved analytically; however, it can be calculated numerically.

Influence of the aperture size

The spread of $p_s(\omega)$ depends on the distance from the scattering surface to the imaging lens z , that is due to the paraxial approximation equal to the distance from the fiber tip to the scattering surface, and the radius of the opening of the imaging aperture a_s . For a given \vec{k}_i , the maximum one-sided Doppler shift is occurred by subtracting the two scattering wavevectors to the center of the pupil and to the side of the pupil as

$$\omega_{D_s} = \vec{v} \cdot (\vec{k}_{s_1} - \vec{k}_{s_2}). \quad (6)$$

Performing the vector product in (6) yields

$$\omega_{D_s} = \frac{2\pi a_s}{\lambda} V. \quad (7)$$

The shape parameter χ_s introduced in (3) is set to the fraction $\frac{a_s}{z}$ in (7) to enable establish a comparison between the theoretical predictions and simulation and experimental results.

Forms of illumination

To study the influence of wavefront types, three common forms are considered namely, planar waves, spherical waves and scrambled waves. For the case of plane waves, all the incoming wavevectors (\vec{k}_i) are of the same direction (see Figure 3(a)). This makes the wavevector density function $p_{-i}(\omega)$ a Dirac delta function (i.e. $\chi_i = 0$). For the case of spherical wave illumination, the incoming wavevectors originate from a point (the optical fiber tip in our case) and take space dependent directions (see Figure 3(b)). However, since only surface scattering occurs on the considered object, only a single wavevector contributes to the occurred Doppler shift. Therefore, the same optical Doppler shift spectrum is expected to be resulted for planar and spherical wave illumination schemes.

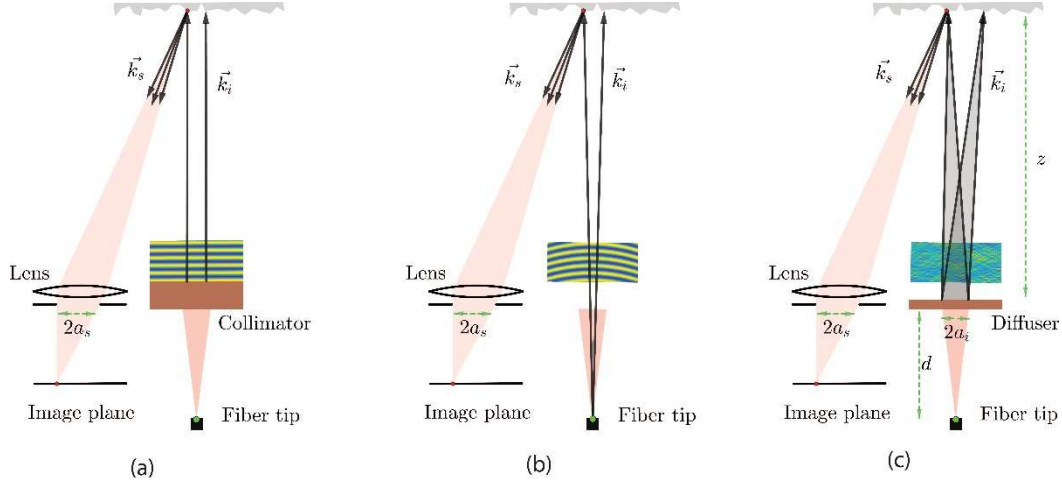


Figure 3 Schematic drawing of (a) plane wave, (b) spherical wave and (c) scrambled wave illumination in the model of the optical system where a very high scattering object (e.g. a matte surface) is considered. This figure is partly adapted from [10].

The case of scrambled wave illumination is realized by passing spherical waves through an engineered diffuser (see Figure 3(c)). Here the distance from the fiber tip to the diffuser d indicates the radius of illuminated area on the diffuser a_i . Similar the influence of aperture size and from the illumination point-of-view, the radius of the illuminated area on the diffuser influences the occurred Doppler shift. For a given \vec{k}_s , the maximum one-sided Doppler shift can be calculated by subtracting the two wavevectors originating from the center and the edge of illuminated area on the diffuser pointing towards the same point on the scattering surface as

$$\omega_{D_i} = \vec{v} \cdot (\vec{k}_{t_1} - \vec{k}_{t_2}). \quad (8)$$

The numerical aperture of the optical fiber is defined as $NA = n \sin(\theta) = \frac{a_i}{d}$ when travelling through air ($n = 1$) and assuming paraxial approximation. Thus, calculating the vector product in (8) gives

$$\omega_{D_i} = \frac{2\pi a_i}{\lambda z} V = \frac{2\pi dNA}{\lambda z} V. \quad (9)$$

The scattering shape parameter χ_s introduced in (3) is set equal to the fraction $\frac{dNA}{z}$ to enable evaluate theoretical prediction of speckle contrast with the simulation and experimental results.

3. METHODS

Simulation of dynamic speckles

A mesh of 128×128 px was created and dynamic speckles were made for each pixel. The complex amplitude for each pixel (x_i, y_i) was made as

$$E(x_i, y_i, t) = \frac{1}{\sqrt{n}} \sum_n A(\omega_n(x_i, y_i)) \exp(i(\omega_n(x_i, y_i)t + \phi_n(x_i, y_i))), \quad (10)$$

where ω_n is a uniformly distributed random frequency within the range of the optical Doppler spectrum introduced in (2) and $A(\omega_n)$ is the corresponding amplitude. ϕ_n is also a uniformly distributed random phase on the interval $[0, \pi]$. n is the number of phasors which is greater than 100. The intensity of each pixel was calculated as $I(t) = |E(t)|^2$. Then, the intensities were time-integrated which an exposure time of $T = 10$ ms. The spatial contrast of each time-integrated intensity frame was calculated as [14]

$$C = \frac{\sigma_I(x, y)}{I(x, y)} \quad (11)$$

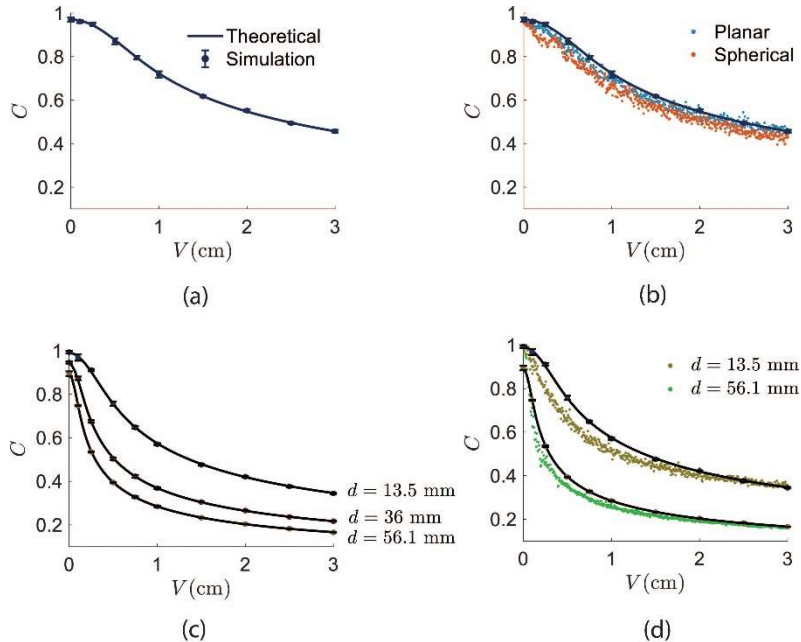


Figure 4 Graphs of speckle contrast versus applied translational speed for the cases of (a-b) planar and spherical waves illumination schemes and (c-d) scrambled waves illumination scheme. (a) and (c) show numerical curves and simulation results for the cases of planar/spherical and scrambled waves illumination schemes, respectively. (b) and (d) show experimental data associated with (a) and (c), respectively.

where $\sigma_I(x, y)$ and $\bar{I}(x, y)$ are spatial standard deviation and mean of the intensities at each frame.

Experimental setup

The in-house handheld LSCI probe was mounted on a translational stage (Zaber X-LHM200A-E03) to apply speeds in the range of 0 – 30 mm/s with an acceleration of 3 mm/s². A metal plate painted with matte color (Ecopaint Vintage chalk paint spray 400 ml) was used as a scattering surface. The laser light (CNI MSL-FN-671, $\lambda = 671$ nm) was coupled to a single mode optical fiber (Thorlabs SM600, $NA = 0.12$). At $z = 20$ cm, from the fiber tip, the beam-width (i.e. the width of the beam for which the intensity reaches $1/e^2$ of its maximum) was measured as 3 cm. At the distal end of the optical fiber on the probe, a pair of plano-concave and achromatic doublet lenses ($f = 6$ cm) were used to make a collimated beam. For the scrambled waves, the pair of lenses were replaced by a 20° top hat diffuser (Thorlabs EDI-s20-MD).

At the detection side, a monochrome camera (Basler acA2040 55um USB3) was used to record speckle patterns with an exposure time of $T = 10$ ms. The camera objective (FUJINON HF16XA-5M) had an f-number of $N = 8$ and a focal length of $f = 16$ mm. Its aperture radius can be calculated as [15]

$$a_s = \frac{f}{2N} = 1 \text{ mm} \quad (12)$$

A linear polarizer (Thorlabs LPNIRE 100-B) with a direction perpendicular to the polarization of laser light was mounted on the camera objective to minimize specular reflection. A bandpass filter (Edmund Optics, $\lambda = 675 \pm 12$ nm) was also mounted on the camera objective to minimize background light. The magnification of the imaging system was measured as the fraction of the image size to the object size, $M = 0.1$. A window of 90×90 px was chosen at the center of scattering spot to calculate spatial speckle contrast as introduced in (11).

4. RESULTS AND DISCUSSION

The contrast of the time-integrated intensity introduced in (5) was used to evaluate the proposed model. The analysis was carried out in two phases, namely the cases of (1) planar and spherical waves illumination and (2) scrambled waves illumination. To do so, an optical Doppler spectrum according to (2) was formed by convolving a pair of wavevector density functions related to the incoming and outgoing vectors with a semi-circular function introduced in (3). Then,

dynamic speckles were made according to (10) and their contrast values were calculated using (11). A comparison between the theoretical prediction of speckle contrast versus applied speed and simulation result for the case of planar and spherical waves illumination is shown Figure 4(a). Such results for scrambled waves illumination is illustrated in Figure 4(c) in which three values for fiber tip to diffuser distances namely $d = \{13.5, 36, 56.1\}$ mm are considered. A precise match between theoretical and simulation curves is obtained for both cases.

In Figure 4(b) speckle contrast is shown versus applied speed for the motorized experiments with planar and spherical waves illumination. The speckle contrast at zero speed is about 0.95 indicating a nearly fully developed speckle pattern. The dropping behavior for both curves is fairly similar. The speckle contrast drop percentages for the pair of (planar, spherical) at the speeds of 1 cm/s are (27.5%, 30.4%) and at the speed of 3 cm/s are (54.3%, 58%). It can be seen that the theoretical curve matches the case of planar waves illumination. However, there is a slight deviation for spherical waves illumination. This can be explained by the fact that in theory and simulation only one \vec{k}_i is assumed contributing to the doppler shift at the detection point (i.e. a Dirac delta function for $p_{-i}(\omega)$). However, in practice, the detection point may not be infinitely small such that a small area including a range of \vec{k}_i is being imaged at a camera pixel. Moreover, the matte surface phantom is not of infinite scattering level as opposed to the assumption in theory and simulation. Therefore, contribution of \vec{k}_i illuminated at other locations than the detection point as a result of volume scattering may be detected at the imaging pixel.

In Figure 4(d), the speckle contrast versus translational speed is shown for the case of scrambled waves illumination for two different fiber tip to diffuser distances. The speckle contrast values are close to unity at zero speed and drop as the applied speed is increased. The larger the distance d , the greater the speckle contrast drop for a given speed. Here the speckle contrast drop percentages for the set of $d = \{13.5, 56.1\}$ mm at the speed of 1 cm/s are {48.3, 71}% at the speed of 3 cm/s are {66.2, 81.5}%.

5. CONCLUSION

In this work, we developed a model to predict movement artefacts resulted by translational motions in handheld laser speckle contrast perfusion imaging. The proposed model is on the basis of the optical Doppler shift distributions correspond to the range of wavevectors for both illumination and detection. It has been shown that the speckle contrast drop as a measure of movement artefacts is a function of the applied translational speed, the form of illumination, and the geometry of imaging system. We have validated this model by simulation of dynamic speckles as well as experiments and an agreement has been found between the theoretical predictions and those obtained by simulations and experiments. What we considered in this work was the cases of illumination with plane waves, spherical waves and scrambled waves on a high scattering surface. In a typical in-vivo LSCI measurement, however, the object of interest would be human skin which has a finite scattering level. Thus, as a future work, it is crucial to extend the study by measuring on phantoms with more realistic optical properties. Results of this research paves the way to enable development of model-based methods that are able to compensate movement artefacts in a handled LSCI.

6. ACKNOWLEDGMENT

This study was supported by the Open Technology program of the Netherlands Organization for Scientific Research (NWO), Domain Applied and Engineering Sciences, under grant number 14538.

7. REFERENCES

- [1] L. Bento, L. Tavera, P. Assuncao, S. Faria and R. Fonseca-Pinto, "Evaluation of cutaneous microcirculation patterns by laser speckle imaging," in *2018 41st International Convention on Information and Communication Technology, Electronics and Microelectronics, MIPRO 2018 - Proceedings*, 2018.
- [2] M. J. Schaap, A. Chizari, T. Knop, H. M. M. Groenewoud, P. E. J. van Erp, E. M. G. J. de Jong, W. Steenbergen and M. M. B. Seyger, "Perfusion measured by laser speckle contrast imaging as a predictor for expansion of psoriasis lesions," *Skin Research and Technology*, 2021.

- [3] J. V. Berggren, K. Tenland, R. Sheikh, J. Hult, K. Engelsberg, S. Lindstedt and M. Malmsjö, "Laser Speckle Contrast Imaging of the Blood Perfusion in Glabellar Flaps Used to Repair Medial Canthal Defects," *Ophthalmic Plastic and Reconstructive Surgery*, 2021.
- [4] K. J. Zheng, E. Middelkoop, M. Stoop, P. P. M. van Zuijlen and A. Pijpe, "Validity of laser speckle contrast imaging for the prediction of burn wound healing potential," *Burns*, 2021.
- [5] B. Lertsakdadet, C. Dunn, A. Bahani, C. Crouzet and B. Choi, "Handheld motion stabilized laser speckle imaging," *Biomedical Optics Express*, vol. 10, p. 5149, 2019.
- [6] J. Zötterman, R. Mirdell, S. Horsten, S. Farnebo and E. Tesselaar, "Methodological concerns with laser speckle contrast imaging in clinical evaluation of microcirculation," *PLoS ONE*, vol. 12, p. 1–11, 2017.
- [7] B. Lertsakdadet, B. Y. Yang, C. E. Dunn, A. Ponticorvo, C. Crouzet, N. Bernal, A. J. Durkin and B. Choi, "Correcting for motion artifact in handheld laser speckle images," *Journal of Biomedical Optics*, vol. 23, p. 1, 2018.
- [8] A. Chizari, M. J. Schaap, T. Knop, Y. E. Boink, M. Seyger and W. Steenbergen, "Handheld versus mounted laser speckle contrast perfusion imaging demonstrated in psoriasis lesions," *Scientific reports*, vol. 11, p. 1–13, 2021.
- [9] A. Chizari, T. Knop, B. Sirmacek, F. van der Heijden and W. Steenbergen, "Exploration of movement artefacts in handheld laser speckle contrast perfusion imaging," *Biomedical Optics Express*, vol. 11, p. 2352–2365, 2020.
- [10] A. Chizari, T. Knop, W. Tsong, S. Schwieters and W. Steenbergen, "Influence of wavefront types on movement artefacts in handheld laser speckle contrast perfusion imaging," *OSA Continuum*, vol. 4, p. 1875–1888, 2021.
- [11] Y. Yeh and H. Z. Cummins, "Localized fluid flow measurements with an He–Ne laser spectrometer," *Applied Physics Letters*, vol. 4, p. 176–178, 1964.
- [12] A. Chizari, "Handheld laser speckle contrast perfusion imaging," University of Twente, Netherlands, 2021.
- [13] F. Bowman, Introduction to Bessel functions, New, York: Dover, 1958.
- [14] J. W. Goodman, Speckle phenomena in optics: theory and applications, Roberts and Company Publishers, 2007.
- [15] B. H. Kolner, "Generalization of the concepts of focal length and f-number to space and time," *Journal of the Optical Society of America A: Optics and Image Science, and Vision*, vol. 11, pp. 3229–3233, 1994.